RSC Advances

PAPER

View Article Online
View Journal | View Issue

Cite this: *RSC Adv.*, 2026, **16**, 20933

Activation of peroxymonosulfate by distillers' grains biochar for the degradation of ciprofloxacin: critical roles of singlet oxygen and electron transfer

Hangdao Qin, *[a] Pei Liu,[a] Junnan Hao,[a] Lei Xiao,[a] Yong Wang,[a] Jiming Huang,[a] Jun Chang,[a] Yuru Shen,[a] Bo Xing[b] and Guo Yang[b]

The distillers' grains biochar was prepared by a simple ball-milled process, followed by pyrolysis at different temperatures. The as-prepared biochars were then utilized to degrade ciprofloxacin (CIP) *via* peroxymonosulfate (PMS) activation. At the optimal pyrolysis temperature of 900 °C, a biochar with a high density of surface defects and a large surface area was generated. Therefore, 100% CIP degradation was attained within 40 min using the DBC900/PMS system. This system also showed good stability across five reuse cycles as well as good performance over a wide range of pH values. The water matrix showed a negligible effect on CIP degradation in this system. Electron paramagnetic resonance (EPR), quenching experiments and electrochemical analysis demonstrated that CIP degradation involved non-radical and electron transfer pathways. The production of $^1O_2$ and electron transfer mediated by the metastable complex DBC900-PMS* were crucially involved in this degradation reaction. Moreover, a possible degradation pathway of CIP was proposed based on the analysis of the intermediate products. Overall, this study provided an enhanced understanding of the biochar-activated PMS mechanism and offered a compelling strategy for the resourceful utilization of waste distillers' grains.

Received 11th March 2026
Accepted 15th April 2026

DOI: 10.1039/d6ra02077a

rsc.li/rsc-advances

1. Introduction

Antibiotics belong to pharmaceuticals and personal care products (PPCPs), and the increasing presence of antibiotics in aquatic environments poses notable environmental and health risks worldwide. Specifically, the diversity of antibiotics, their wide environmental distribution, potential toxicity, persistence, and poor biodegradability threaten human health and the stability of ecosystems.[1] The third-generation fluoroquinolone antibiotic ciprofloxacin (CIP) is frequently utilized to treat infections caused by microorganisms resistant to other antibiotic compounds.[2] The strong environmental persistence and poor biodegradability of CIP contribute to its long-term environmental persistence.[3] Therefore, effective measures must be developed to efficiently degrade CIP in water.

Sulfate radical-based advanced oxidation processes (SR-AOPs) are compelling due to their affordability, stability, low toxicity, and degradation pathway diversity.[4] Typically, radical-based pathways involve the formation of radicals that are highly reactive but not very selective, mainly sulfate radicals ($SO_4^{\bullet-}$) and hydroxyl radicals ($^{\bullet}OH$). This lack of selectivity notably hinders the practical application of these strategies due to the indiscriminate reaction between $SO_4^{\bullet-}$/$^{\bullet}OH$ and water matrix components, such as natural organic matter (NOM) and inorganic ions.[5,6] Non-radical pathways, including singlet oxygen ($^1O_2$) generation, electron transfer and hypervalent metal oxidation, have gained increasing interest due to its robustness against inorganic anions and NOM, along with its high selectivity in degradation applications.[7,8]

The pursuit of non-radical pathways in SR-AOPs has spurred the development of diverse catalysts. Metal-free carbonaceous materials can be employed for physicochemical property regulation, triggering non-radical degradation pathways.[9] For example, graphitic carbon nitride was employed to prepare nitrogen-doped carbon nanosheets, which were used to activate PMS and generate $^1O_2$. These nanosheets displayed improved catalytic performance for bisphenol A degradation.[10] Biochar (BC) was a promising candidate for practical applications because it exhibits modifiable surface functionalities, has a hierarchical pore structure, and consists of a conductive carbon matrix. Algal biochar was synthesized and applied toward peroxydisulfate (PDS) activation as a metal-free catalyst. A mechanistic study indicated that $^1O_2$ and the electron transfer pathway were critically involved in the degradation of enrofloxacin (ENR) by this biochar.[11] Waste pumpkin seed pomace was used as a raw material to synthesize a pristine biochar material for activating PDS, enabling rhodamine B (RhB) to be degraded and mineralized. Quenching experiments revealed that RhB degradation was primarily caused by the reactive oxygen species $^1O_2$.[12]

[a]*School of Material and Chemical Engineering, Tongren University, Tongren 554300, China. E-mail: qinhangdao@126.com*

[b]*College of Chemical Engineering, Sichuan University of Science and Engineering, Zigong 643000, China*

The liquor industry generates distillers' grains as a solid waste material. Notably, China's yearly production of distiller's grains is greater than 100 million tons.[13] The main components of this waste product are cellulose, hemicellulose and lignin, indicating its suitability for biochar production.[14] To date, the distillers' grains biochar has been evaluated for the removal of heavy metal, phosphates, dyes and antibiotics.[15–18] Distillers' grains biochar can capably adsorb these target contaminants due to its tunable porosity, large specific surface area, low price and environmental friendliness.[19] Still, few study are available on the utilization of distillers' grains biochar for catalytic AOP-based organic pollutant degradation.

The use of metal-free carbon-based catalysts for PMS activation to degrade organic pollutants has been widely investigated.[20–22] However, strategies employing distillers' grains biochar for effectively degrading CIP have not yet been reported. Herein, the goal of this study is the development of a metal-free biochar/PMS system for aqueous CIP degradation. First, distillers' grains biochar was synthesized through ball-milling and pyrolysis, and the physicochemical characteristics and surface properties of the biochar were systematically evaluated. The performance of distillers' grains biochar prepared under various pyrolysis temperatures was studied, and the optimal reaction conditions (catalyst dose, concentration of PMS, pH, and reaction temperature) were identified. Then, the reactive oxygen species involved in degradation were identified and the PMS activation mechanism was elucidated. Finally, the catalyst's reusability, stability, universality resistance to water matrix interference were evaluated. By advancing a mechanistic understanding of PMS activation by distillers' grains biochar, this work provides a sustainable option for the valorization of distillers' grains.

2. Experimental

2.1. Materials and chemicals

Distillers' grains were provided by a liquor factory in Tongren (Tongren, China). Ciprofloxacin was acquired from Aladdin Reagent Co., Ltd (Shanghai, China). Additional chemicals were provided by Sinopharm Chemical Reagent Co., Ltd, China.

2.2. Preparation and characterization of distillers' grains biochar

To remove impurities, distilled water was used to wash the distillers' grains several times. After oven drying at 110 °C, the distillers' grains were ball-milled to obtain a fine powder and sieved to −100 mesh. Next, the powders were loaded in a quartz tube furnace and pyrolyzed under a N_2 flow at 500 °C, 700 °C and 900 °C for 2 h (10 °C min^{-1} ramp rate) to prepare biochar samples. These biochar samples were denoted as DBC500, DBC700 and DBC900 based on the pyrolysis temperature. Further characterization information is detailed in Text S1 of the SI.

2.3. CIP degradation and analysis

Batch CIP degradation was achieved in 250 mL conical flasks loaded with 100 mL of CIP solution (20 mg L^{-1}) and a specified catalyst dosage. The mixture was then reacted in an air bath shaker at a constant temperature of 25 °C and 150 rpm. Then, a certain dose of PMS was added, initiating the degradation of CIP. Samples were obtained at regular intervals and immediately filtered using a 0.22 μm membrane.

High-performance liquid chromatography (HPLC, Shimadzu, LC-20A) using a C18 column (4.6 × 250 mm, 5 μm) and UV detector was employed to determine the CIP concentration. A mixture of acetonitrile and 0.1% formic acid aqueous solution (25 : 75, v/v) was used as the mobile phase, detection was carried out at a wavelength of 280 nm, and a 1.0 mL min^{-1} flow rate was utilized. Total organic carbon values were measured by a TOC-L CPN Total Organic Carbon Analyser (Shimadzu, Japan).

A CHI660E A23760 electrochemical workstation (Shanghai Chenhua Instrument Co., Ltd) was employed for electrochemical analyses, including cyclic voltammetry (CV), open circuit potential (OCP), linear sweep voltammetry (LSV), and electrochemical impedance spectroscopy (EIS). A 0.2 M Na_2SO_4 electrolyte was employed for the CV, OCP, LSV, and EIS analyses. Platinum, glassy carbon drop-coated with the catalyst, and Ag/AgCl were employed as the counter, working, and reference electrodes in a conventional three-electrode setup.

3. Results and discussion

3.1. Characterization of DBC

Morphological observations of the distillers' grains biochar were obtained by SEM. DBC500 (Fig. 1a and b) had a relatively smooth surface, and a minimal surface erosion was found. In contrast, DBC700 (Fig. 1c and d) had a partly irregular blocky structure, peeling off from the lumpy carbon (Fig. 1c and d). Meanwhile, DBC900 (Fig. 1e and f) had noticeable surface erosion and observable pore structures.

The biochar crystal structures were studied using XRD (Fig. 2a). A broad peak located at 23.9° was found for all the three samples, which was ascribed to the (002) plane of graphite and indicated the formation of amorphous carbon structure. Another diffraction peak ascribed to the graphite (111) plane was observed at 43.4°. Meantime, it was found that the biochar samples contained quite a lot of impurities, such as SiO_2 and $CaCO_3$. The similar results were reported in the previous study.[23] As the pyrolysis temperature was raised, these mineral peak intensities were enhanced, and peak sharpness increased. Moreover, higher pyrolysis temperature could lead to the greater carbonization of the distillers' grains biochar, leading to higher crystallinity and a more stable structure.[24]

Fig. 2b illustrated the FT-IR spectra of DBC500, DBC700 and DBC900. The peak at 3427 cm^{-1} was potentially related to O–H stretching vibrations, while those at 2890 and 2973 cm^{-1} respectively corresponded to aliphatic C–H symmetric and asymmetric stretches. Aromatic C=C ring stretching (caused by aromatization) was indicated by the peak at 1445 cm^{-1}, and aromatic C=C and C=O stretching vibrations were demonstrated by the 1631 cm^{-1} peak. The 1049 cm^{-1} peak corresponded to the stretching vibration of aryl ether C–O–C bonds. The presence of these bonds was attributed to the thermal decomposition of cellulose, ester C=O, aliphatic alkyl,

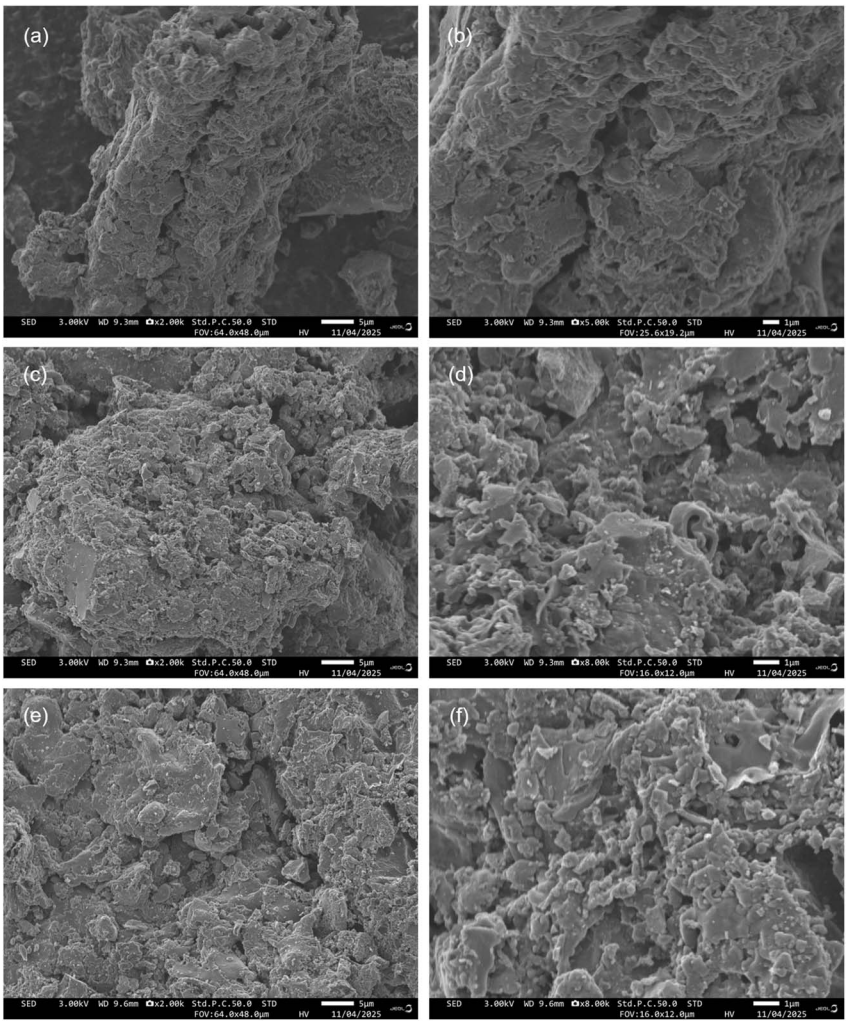

Fig. 1 SEM micrographs of DBC500 (a and b), DBC700 (c and d) and DBC900 (e and f).

aromatic C═O and –OH groups as well as the aromatic structures remaining in the lignin residue being exposed.[25] Out-of-plane aromatic deformation was responsible for the C–H bending peak at 881 cm^{-1}. Moreover, by contrasting the spectra, it could be seen that the peak for aromatic C═C and C═O at 1631 cm^{-1} gradually increased as the pyrolysis temperature increased. This observation implied that more intense pyrolysis resulted in the greater aromatization of the biochar.[20]

The structures of DBC500, DBC700 and DBC900 were also characterized by Raman spectroscopy (Fig. 2c). Two prominent characteristic signals at 1350 and 1592 cm^{-1} represented lattice defects (D band) and graphitic structure (G band). The degree of defects in the three biochar samples was compared using the intensity ratio of these peaks (I_D/I_G).[26] As listed in Table 1, the I_D/I_G value was calculated to be 0.847, 0.927 and 0.989 for DBC500, DBC700 and DBC900, respectively. Higher I_D/I_G values were observed as the pyrolysis temperature was raised, which indicated a greater prevalence of defects and disordered carbon structures in DBC900. This might be ascribed to the organic compounds thermally decomposing at high temperatures, disrupting original carbon lattice and promoting the formation of structural defects.

N_2 adsorption–desorption was utilized to study the porosity of the three biochars (Fig. S1a of the SI). DBC900 showed a type IV isotherm with an H3 hysteresis loop, demonstrating the existence of mesoporosity. The pore size distributions in Fig. S1b further confirmed this observation. DBC500 and DBC700 had very low BET specific surface areas (S_{BET}) of just 0.82 and 3.17 $m^2\ g^{-1}$, respectively (Table 1). However, when the pyrolysis temperature reached 900 °C, the S_{BET} and total pore volume (V) sharply increased to 736 $m^2\ g^{-1}$ and 0.47 $cm^3\ g^{-1}$. This significant enhancement of S_{BET} and V was potentially caused by the higher pyrolysis temperature inducing the removal of impurities and release of volatile component, which promoted the production of pores and enhanced the surface area. This result was in agreement with the morphological analysis (Fig. 1).

As shown in Fig. 2d, the surface elemental compositions and valence states of the three biochar samples were studied using XPS. The C 1s, N 1s and O 1s peaks were respectively located at 284.5 eV, 398.5 eV and 532.2 eV. The oxygen content

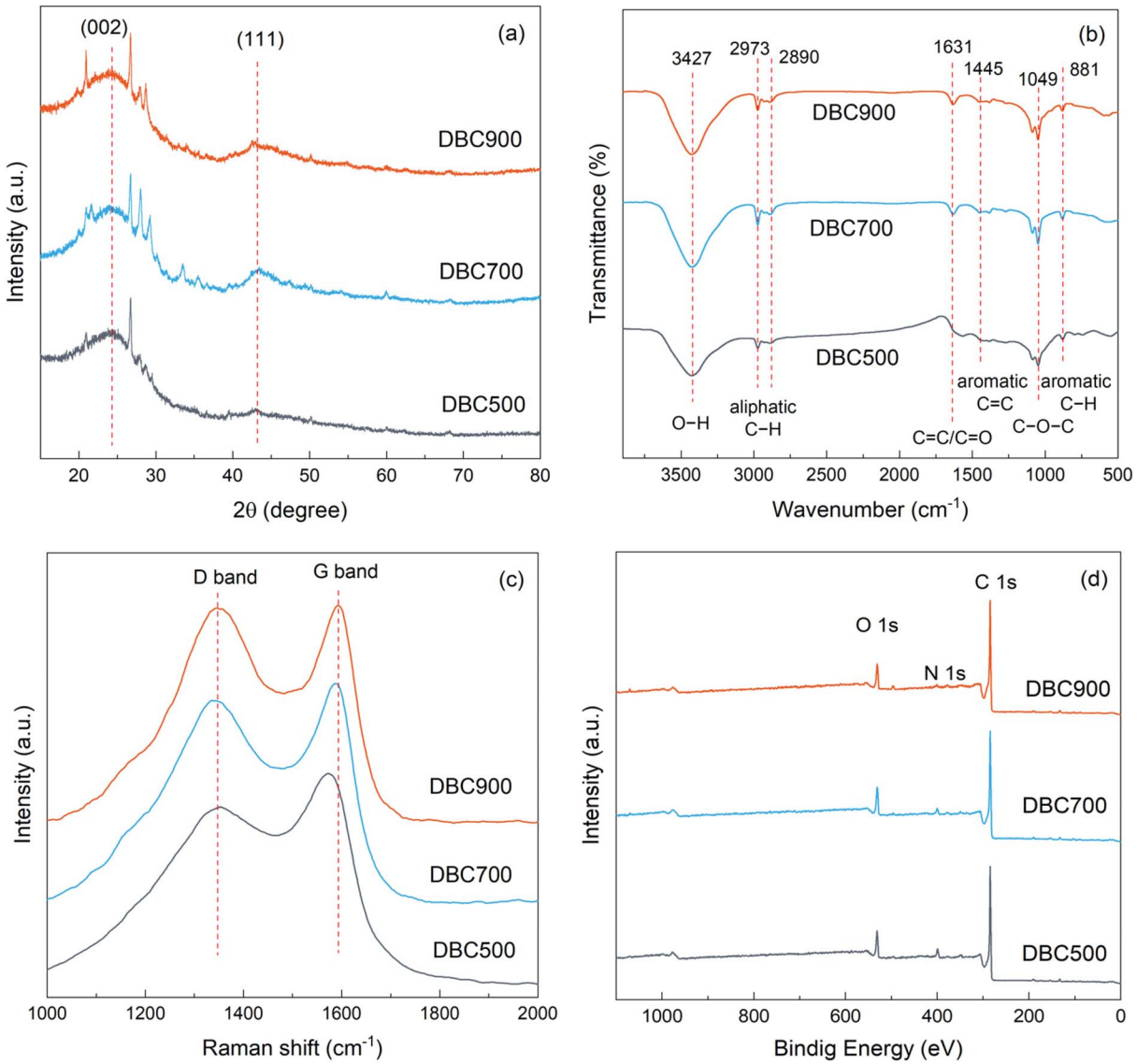

Fig. 2 XRD spectra (a), FT-IR spectra (b), Raman spectra (c) and full XPS spectra (d) of DBC500, DBC700 and DBC900.

Table 1 Typical material properties of DBC500, DBC700 and DBC900

Catalyst	I_D/I_G	S_{BET} ($m^2\ g^{-1}$)	V ($cm^3\ g^{-1}$)
DBC500	0.847	0.82	0.0031
DBC700	0.927	3.17	0.0068
DBC900	0.989	736	0.47

progressively increased with increasing pyrolysis temperature, while a decline in the nitrogen content was observed. This result was attributed to the breakage and conversion of nitrogen-containing species, which released nitrogen from the biochar samples at higher temperatures.[27]

The high-resolution C 1s spectra of the samples (Fig. 3a, c and e) revealed distinct C–C/C=C (284.4 eV), C–O (285.1 eV), C=O (288.2 eV) and π–π* (292.3 eV) peaks. An apparent enhancement in C=O and π–π* contents was observed with increasing pyrolysis temperature. The enhanced pyrolysis temperature promoted the transformation of C–O to C=O, leading to better thermal stability.[28] The increased C=O ratio also indicated greater aromaticity in the biochar samples.[29] Additionally, other studies have also verified that raising the pyrolysis temperature contributed to the production of π–π* satellite.[10,30]

DBC500, DBC700 and DBC900 showed two O 1s peaks located at 531.0 eV (C–O) and 532.8 eV (C=O) (Fig. 3b, d and f). In agreement with the trend observed in the C 1s spectra, raising the pyrolysis temperature from 500 °C to 900 °C caused the C=O content to increase from 5.6% to 37.2%.

The combined characterization from SEM, FT-IR, Raman spectra, N_2 adsorption–desorption isotherms and XPS provided a comprehensive understanding of how the pyrolysis temperature affected the physicochemical properties on distillers' grains biochar. High pyrolysis temperature effectively removed

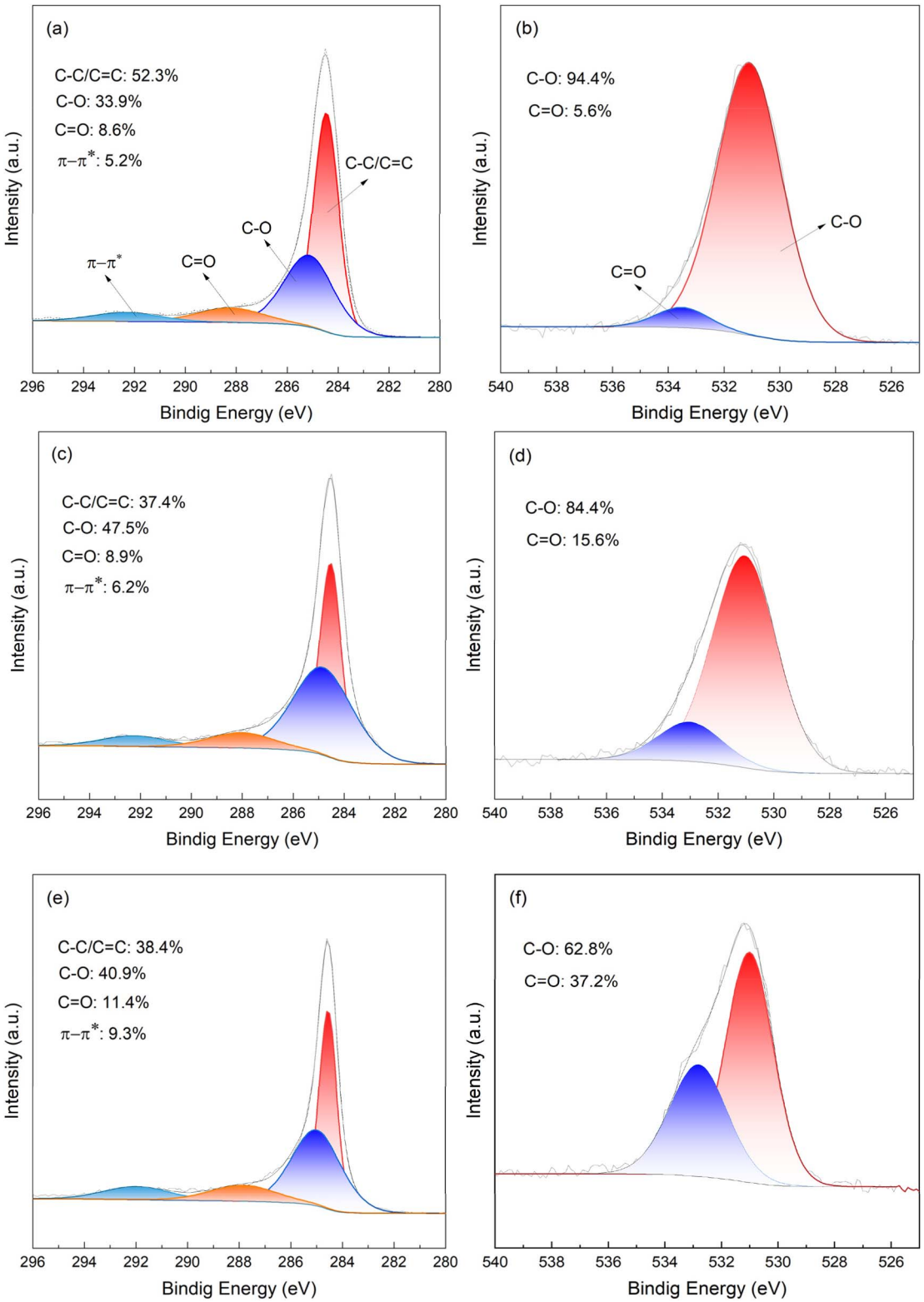

Fig. 3 C 1s and O 1s XPS spectra of (a and b) DBC500, (c and d) DBC700 and (e and f) DBC900.

impurities, tar, volatile components, and minerals from distillers' grains, generating a biochar with abundant aromatic structures and high porosity. Moreover, the degree of aromatization, the degree of defects, surface area, pore volume and C=O content increased observably as the pyrolysis temperature was raised, which underscored the importance of heat-treatment conditions in regulating the properties of biochar materials for specific applications.

3.2. Catalytic performance evaluation

Fig. 4a provided a comparative study of the adsorption of CIP by DBC500, DBC700 and DBC900 over 60 min. The results indicated that the adsorption capacities of DBC500 and DBC700 were approximately 16.7% and 20.3%, while DBC900 exhibited 29.1%. The highest adsorption performance of DBC900 could be attributed to its highest S_{BET} (Table 1). The CIP degradation performance in various systems was illustrated in Fig. 4b. Single PMS exhibited a limited oxidative ability, resulting in a CIP degradation of 30.0%. Notably, the addition of distillers' grains biochar facilitated high CIP decomposition efficiency, which confirmed that PMS activation induced by distillers' grains biochar contributed to CIP degradation. The CIP removal efficiency in DBC500/PMS and DBC700/PMS systems were 45.5% and 72.4 after 60 min of reaction, respectively. Especially, the CIP was almost completely degraded within 40 min in DBC900/PMS system. These findings highlighted the enhanced PMS activation capability of DBC900 for reactive oxygen species (ROS) generation. Moreover, as shown in Fig. 4c, the best TOC removal efficiency of 41.6% was attained by the DBC900/PMS system, which further comfirmed the its superior efficiency in mineralization. However, although the CIP was substantially degraded, a significant amount of reaction byproducts was still not easily oxidized after 60 min.

Fig. 4d and e demonstrated the influence of catalyst dose and PMS dosage on CIP degradation, respectively. 84.4% CIP degradation was attained in 40 min using a DBC900 dose of 1.0 g L^{-1}, and this was improved to 100% efficiency by raising the dose to 2.0 g L^{-1}. Further raising the catalyst dosage to 3.0 g L^{-1} did not lead to any additional improvements. Therefore, for economic reasons, a 2.0 g L^{-1} catalyst dosage was selected in subsequent experiments. Similarly, when the PMS dosage exceeded 2.0 g L^{-1}, the degradation performance hardly changed. Therefore, 2.0 g L^{-1} PMS was used in subsequent experiments.

Solution pH critically influences PMS activation and degradation efficiency. Therefore, the degradation of CIP by DBC900/PMS at various pH levels was investigated (Fig. 4f). In this case, the pH level did not significantly influence the CIP degradation efficiency. The CIP degradation efficiency reached 96.8% and 97.5% even at extremely acid pH (3.38) and basic pH (11.29), respectively. Therefore, the DBC900/PMS system achieved superb CIP degradation performance from pH values of 3.38 to 11.29, which indicated a wide pH range of applicability of this system. Moreover, compared to other biochars, DBC900 exhibited relatively wide pH range of applicability. The alkali-activated algal biochar was not suitable for the application in water of solution pH > 11.0.[11] While a biochar-derived horse manure exhibited superior degradation performance of sulfamethoxazole (SMX) under mildly alkaline or neutral pH conditions, the removal of SMX was significantly inhibited at extremely basic pH (11.0).[29] In the degradation of 1,4-dioxane, pine needle-based biochar achieved degradation efficiencies below 50% at pH 9.0 and 11.0.[25] This contrast demonstrated the excellent promise of the DBC900/PMS system for organic pollutant removal in acid wastewater and alkaline wastewater.

3.3. Effect of water matrix and adaptability test

The ability of the DBC900/PMS system to remove CIP in real water samples was studied by investigating the influence of certain inorganic anion species and NOM on the CIP removal. The presence of $H_2PO_4^-$, HCO_3^-, Cl^- and humic acid (HA, a representative NOM) only negligibly affected the degradation of CIP (Fig. 5a). The co-existence of the anions and HA influenced PMS activation, affecting the pollutant removal efficiency in radical-dominated systems.[31] Therefore, the negligible effect of water matrix on the DBC900/PMS system indicated the greater dominance of singlet oxygen ($^1O_2$) and the electron transfer reaction.[32]

Tap water and lake water (from Mingde Lake in Tongren University, Tongren) were also employed as water matrixes for CIP degradation. The general parameters including pH, TOC and Cl^- of different water bodies were presented in Table S1. As presented in Fig. 5b, CIP degradation efficiencies in lake water and deionized water were comparable, and a small decline to 89.5% was observed in tap water, which could be attributed to the slight effect of Cl^- (Fig. 5a).

The reusability of DBC900 was investigated in cyclic CIP degradation experiments (Fig. 5c). The CIP degradation efficiency only decreased slightly after five cycles, and the degradation efficiency of the fifth cycle was still as high as 86.6%. The results suggested a good stability of DBC900 catalyst.

Finally, to assess the universality of DBC900/PMS system, other PPCPs, including tetracycline (TC), ethylparaben (EtP) and carbamazepine (CBZ), were degraded in the same conditions. As shown in Fig. 5d, TC could be completely removed with 10 min. The degradation efficiency of EtP reached 100% after the reaction of 60 min. CBZ was difficult to degrade, showing a removal rate of 83.9% at 60 min, and the degradation efficiency could further improve under the optimal conditions.

These findings demonstrated that the DBC900/PMS system was sustainable and universally applicable, and its catalytic degradation performance was minimally affected by environmental factors, which was conducive to its utilization in real-world water treatment applications.

3.4. Catalytic mechanism

3.4.1. Identification of ROS. EPR and scavenging analyses were performed to study the mechanism of PMS activation and the CIP degradation pathway in the DBC900/PMS system. EPR tests were utilized to directly determine the ROS generated using the spin-trapping agents 5,5-dimethyl-1-pyrrolidine N-oxide (DMPO) and 2,2,6,6-tetramethyl-4-piperidone (TEMP). The DMPO oxidation product (5,5-dimethyl-2-oxo-pyrroline-1-oxyl, DMPO-X) was indicated by signals with the intensity ratio 1 : 2: 1 : 2: 1 : 2 : 1 (Fig. 6a). As presented in Fig. 6b, a DMPO-$O_2^{\bullet-}$ adduct signal was not observed, confirming that $O_2^{\bullet-}$ was not participated in the degradation of CIP. The main function of $O_2^{\bullet-}$ was to quickly generate $^1O_2$, indicating that this was not the main species influencing the reaction.[29] Meanwhile, typical TEMP-$^1O_2$ 1 : 1 : 1 triplet signals were observed (Fig. 6c), demonstrating the production of $^1O_2$ in the DBC900/PMS system. With increasing reaction time, the

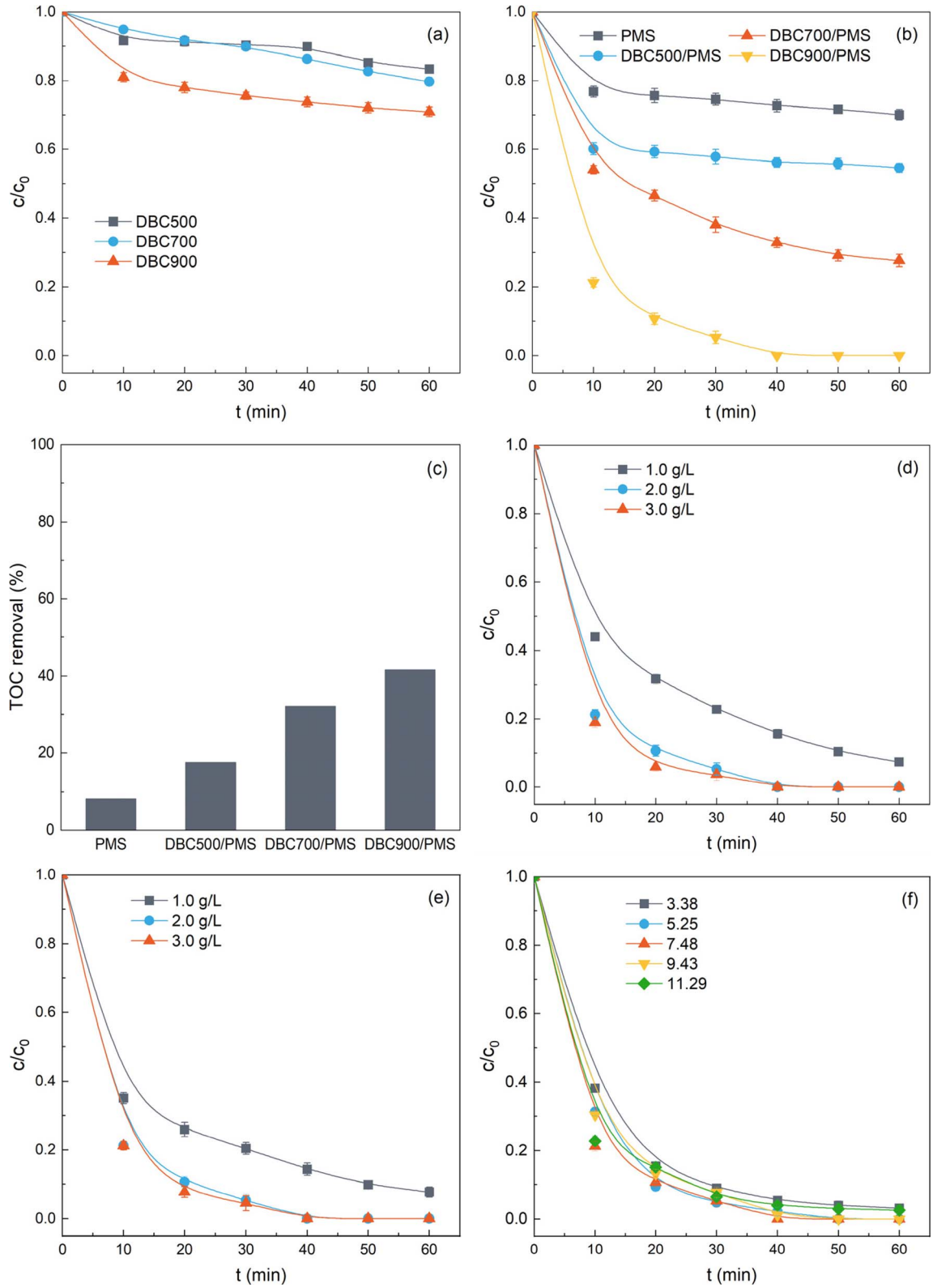

Fig. 4 (a) CIP removal by adsorption; (b) CIP degradation and (c) TOC removal efficiencies in different systems; (d) effect of catalyst dosage in the DBC900/PMS system; (e) effect of PMS dosage in the DBC900/PMS system; (f) Effect of initial pH in the DBC900/PMS system. Reaction conditions: $[CIP]_0 = 20$ mg L^{-1}, $[PMS]_0 = 2.0$ g L^{-1}, $[catalyst]_0 = 2.0$ g L^{-1}, pH = 7.48, $T = 25$ °C.

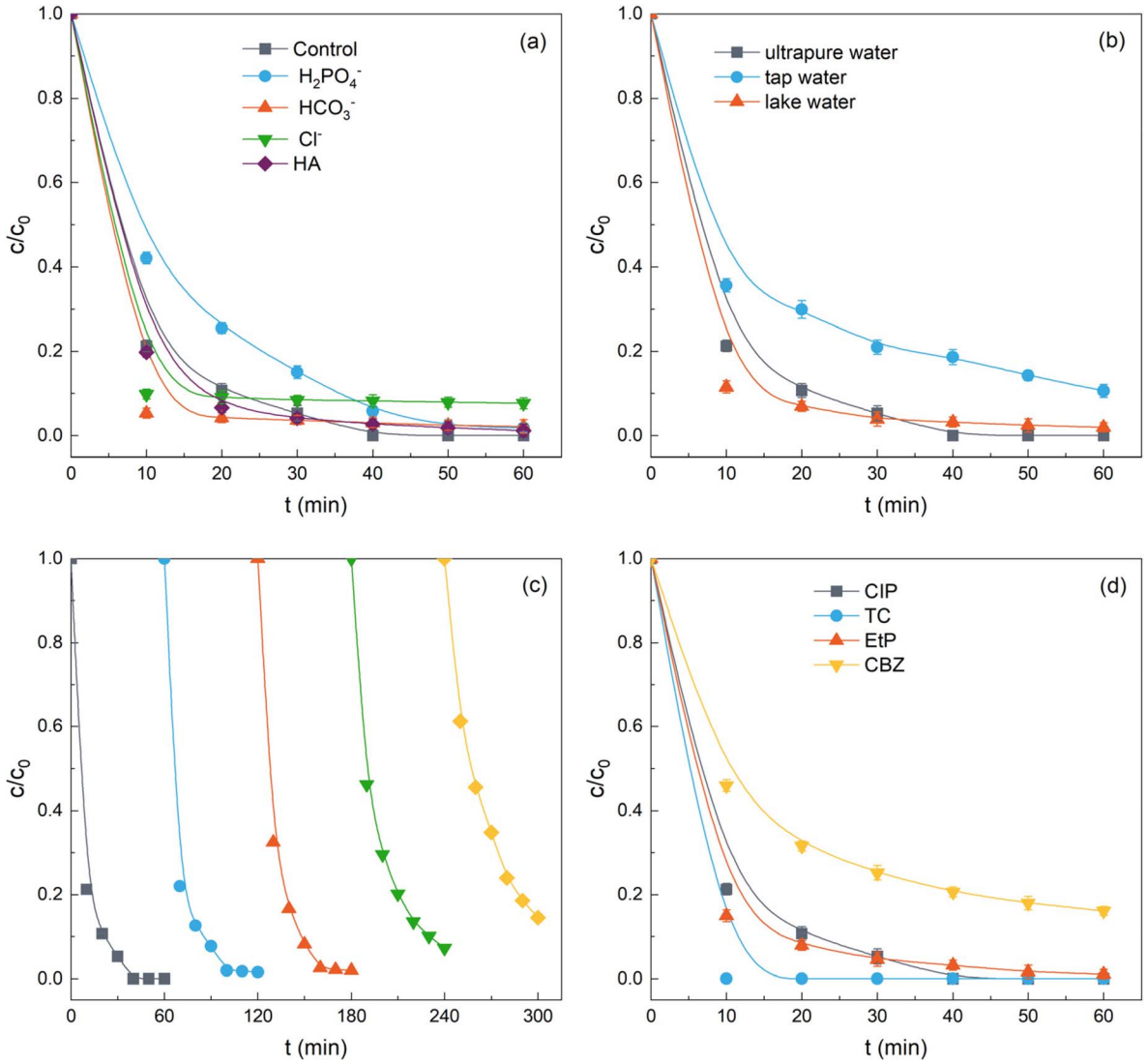

Fig. 5 (a) CIP degradation in the presence of HA or an inorganic anion; (b) CIP degradation in various water matrixes; (c) investigation of reusability of DBC900; (d) DBC900/PMS performance for removing different pollutants. Reaction condition: $[CIP]_0 = 20$ mg L^{-1}, $[PMS]_0 = 2.0$ g L^{-1}, $[catalyst]_0 = 2.0$ g L^{-1}, $[H_2PO_4^-]_0 = [HCO_3^-]_0 = [Cl^-]_0 = = 10$ mmol L^{-1} (if any), $[HA]_0 = 10$ mg L^{-1} (if any), pH = 7.48, $T = 25$ °C.

intensity of the DMPO and TEMP adduct signals increased (Fig. 6a and c), indicating that the system continuously generated $SO_4^{\bullet-}$, $^{\bullet}OH$ and $^1O_2$.

As shown in Fig. 6d, the potential ROS for CIP degradation by the DBC900/PMS system were further identified through quenching experiments. Tert-butanol (TBA) was utilized as a quencher for $^{\bullet}OH$, and ethanol (EtOH) was applied to quench both $SO_4^{\bullet-}$ and $^{\bullet}OH$; benzoquinone (BQ) and L-histidine (L-H) were employed as quenching agent for $O_2^{\bullet-}$ and $^1O_2$, respectively. The addition of each free radical inhibitor (TBA, EtOH and BQ) only led to a slight decline in the degradation efficiency of CIP. In contrast, introducing the non-free radical inhibitor (L-H) significantly suppressed CIP degradation. This finding indicated CIP degradation in the DBC900/PMS system mainly involved $^1O_2$ as the predominant ROS.

Moreover, when dimethyl sulfoxide (DMSO), a surface-bound radical scavenger, was added, a decline in the CIP degradation efficiency from 100% to 69.8% was achieved, confirming that catalytic CIP degradation might involve surface-bound radicals.[33] EPR tests indicated that $SO_4^{\bullet-}$ and $^{\bullet}OH$ were formed in the reaction system, but the quenching experiments indicated that the CIP degradation was minimally affected when adding the quenching agents for $SO_4^{\bullet-}$ and $^{\bullet}OH$. On the other hand, TBA and MeOH were hydrophilic free radical scavengers, only capable of quenching the free radical species in the bulk solution. These scavengers were only minimally able to adsorb onto hydrophobic surfaces to quench surface-bound radical species.[34] Therefore, $SO_4^{\bullet-}$ and $^{\bullet}OH$ were more likely to exist as surface-bound radicals.

Overall, these results demonstrate that various ROS, including $SO_4^{\bullet-}$, $^{\bullet}OH$ $^1O_2$, were generated in the DBC900/PMS system. Surface-bound $SO_4^{\bullet-}$ and $^{\bullet}OH$ might be involved in CIP degradation on catalyst surface, while the significant

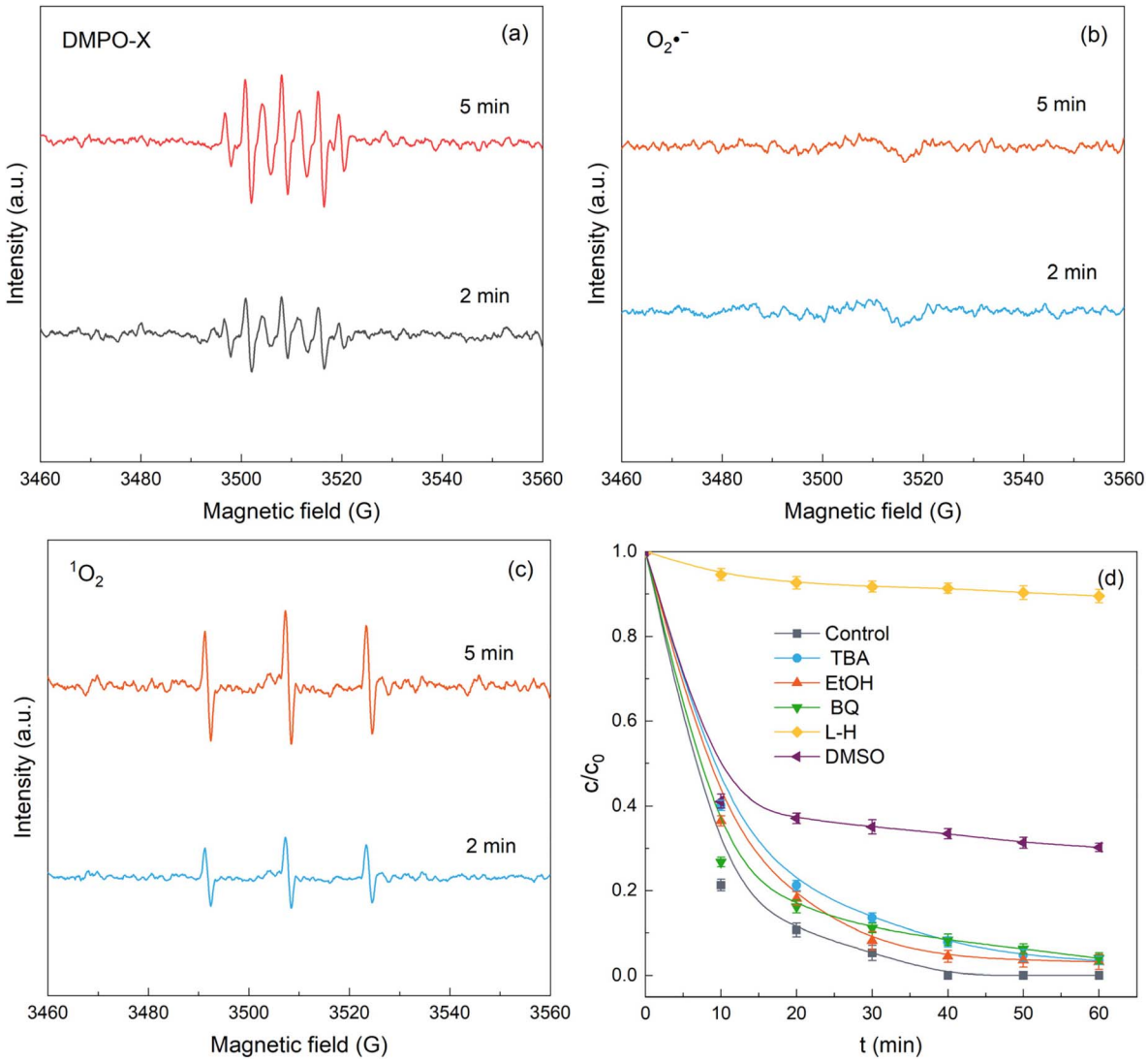

Fig. 6 EPR spectra obtained using (a and b) DMPO and (c) TEMP as spin-trapping agents under different reaction time; (d) quenching experiments in the DBC900/PMS system.

generation of $^1O_2$ in the bulk solution notably contributed to the degradation of CIP.

3.4.2. Confirmation of electron transfer pathway. Electrochemical analyses were performed using glassy carbon electrodes loaded with distillers' grains biochar as the working electrode to study the electron transfer process in the DBC900/PMS system. According to the OCP curves (Fig. 7a), when DBC900 acted as the working electrode, introducing PMS immediately led to an increase in the open-circuit potential. This might be attributed to electrons transferring between PMS and DBC900 to form a metastable intermediate (DBC900-PMS*).[11] With the further introduction of CIP, the potential signal showed a noticeable fluctuation, which was due to the direct electron extraction from the adsorbed CIP by the DBC900-PMS* complex.[11] Therefore, direct electron transfer was involved in CIP degradation in the DBC900/PMS system. Moreover, DBC900 exhibited the highest OCP value of the three biochar samples, providing a better interfacial electron transfer environment.[9,11]

EIS was utilized to assess the conductivity of the biochars, and the EIS Nyquist plots were shown Fig. 7b. By comparison, it could be seen that DBC900 exhibited the smallest semicircle diameter, suggesting it possessed the lowest impedance as well as a strong electron transfer and storage capability. Besides, the CV curves (Fig. 7c) showed that the integrated area were in a sequence of DBC900 > DBC700 > DBC500. This result indicated DBC900 had the most capacitive property and could transfer and store more electrons, providing higher catalytic performance in the system.[9,11]

LSV tests (Fig. 7d) were also used to investigate the charge transfer among DBC900, PMS and CIP. After adding PMS, an increase in current was observed, signifying the interaction between DBC900 and PMS to form DBC900-PMS* complex. The further addition of CIP triggered again an increase in current, indicating the formation of a reactive current from CIP to

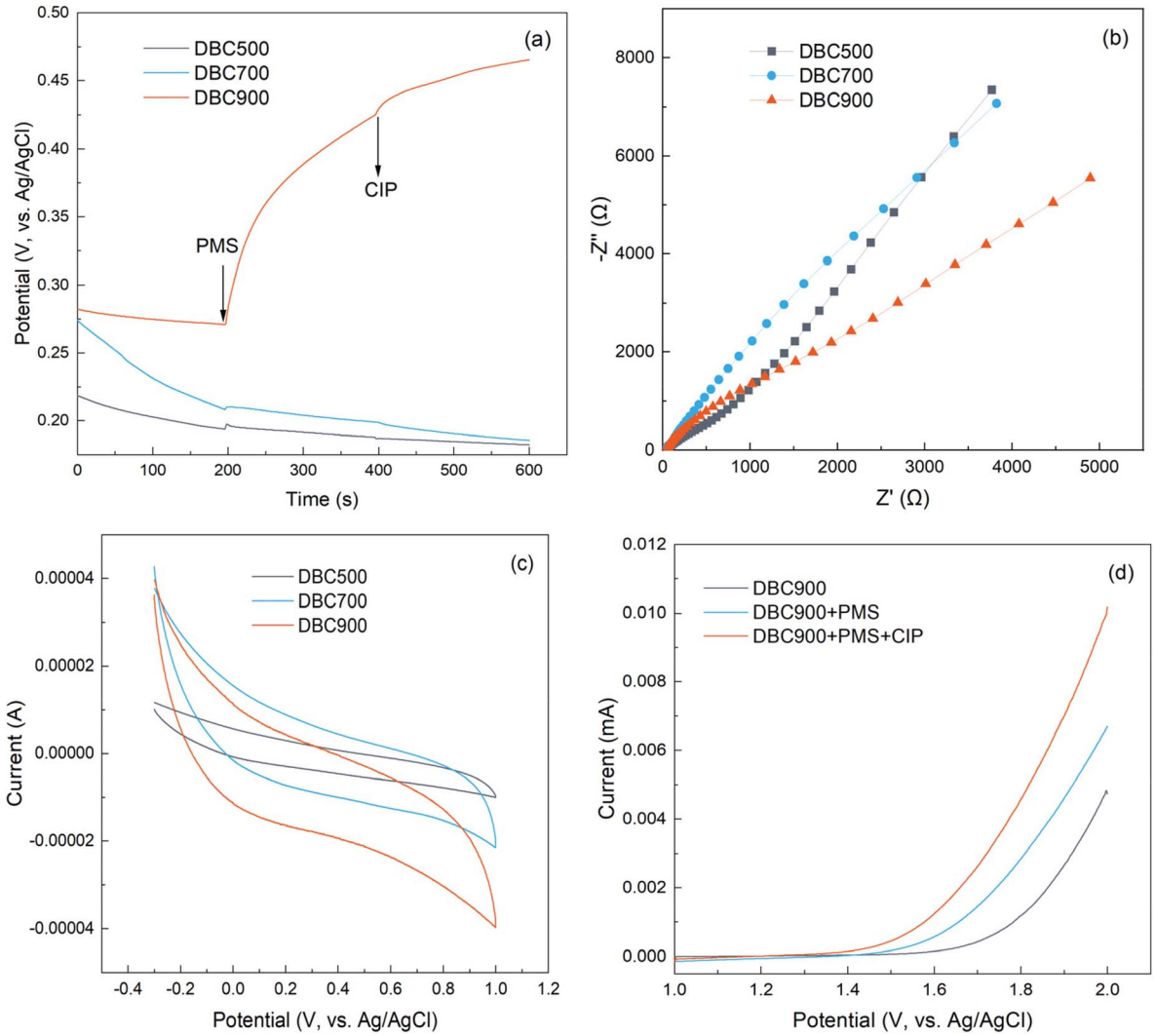

Fig. 7 (a) OCP curves; (b) Nyquist plots; (c) CV curves; (d) LSV curves of different systems.

DBC900-PMS* complex. This was in agreement with the OCP analysis (Fig. 7a).

3.4.3. Investigation of reaction sites. The Raman and XPS spectra of fresh and post-reaction DBC900 were compared to identify the reactive sites in the DBC900. After catalytic CIP degradation, the I_D/I_G value decreased from 0.989 to 0.915 (Fig. 8a), which indicated the defects in DBC900 were significant active sites in the catalysis process. The defects in carbon materials can enhance the PMS activation efficiency through electron transfer.[35] The defective carbon structures in DBC900 decreased after the reaction, leading to a decline in the catalytic degradation efficiency.

The full XPS spectra of DBC900 before and after reaction did not show any notable changes (Fig. 8b), which could explain the result of the stability of DBC900. The C 1s spectra (Fig. 8c) showed a decrease in C=O content from 11.4% to 7.2%, and the π–π* satellite disappeared. Meanwhile, it also could be observed from Fig. 8d that C=O content was sharply decreased from 37.2% to 8.1%. These results indicated highlights C=O in DBC900 was crucially involved in this catalytic reaction. On the one hand, hexagonally networked C=O groups can directly generate $^1O_2$ *via* persulfate activation.[36] On the other hand, the lone pair electrons in the ketonic C=O Lewis base could enhance the density of electrons around nearby carbon atoms, contributing to transfer of electrons between DBC900 and PMS.[37]

Based on the experimental results, a possible catalytic CIP degradation pathway in the DBC900/PMS system was proposed. CIP was mainly degraded through non-radical pathway and electron transfer pathway. In the non-radical pathway, PMS activation proceeded *via* the ketonic C=O in DBC900 to generate $^1O_2$ (Eq. (1)). Moreover, defects in DBC900 could activate PMS to produce $O_2^{\bullet-}$, and then $O_2^{\bullet-}$ immediately reacted with H_2O to produce $^1O_2$ (eqn (2) and (3)). In the electron transfer pathway, DBC900 interacted with PMS to form DBC900-PMS*, a metastable active species. In this interaction, the electron donor CIP transferred electrons to DBC900-PMS*, resulting in CIP degradation while generating surface-bound $SO_4^{\bullet-}$ and $^{\bullet}OH$ (eqn (4) and (5)).

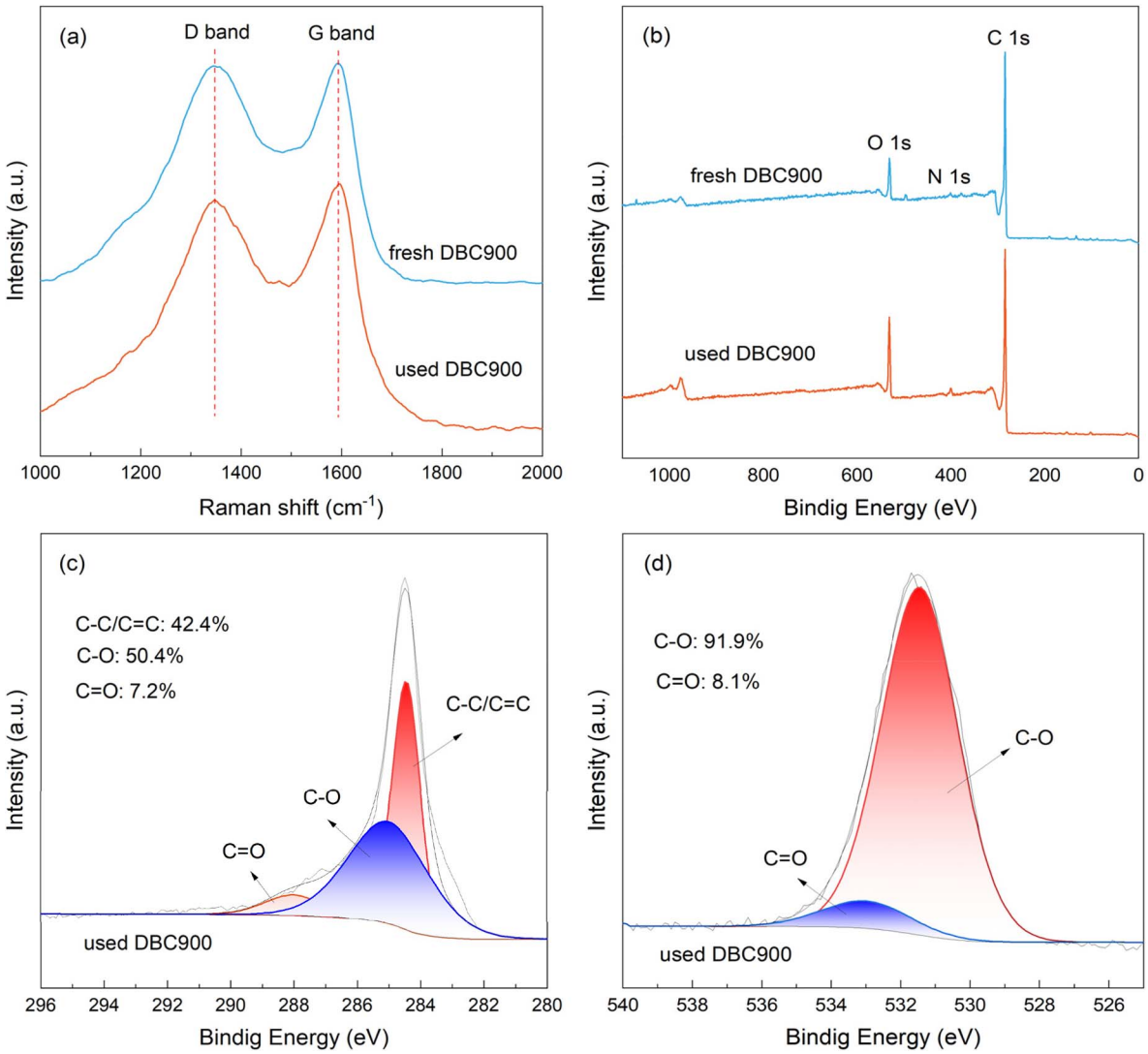

Fig. 8 (a) Raman spectra and (b) full XPS spectra of DBC900 before and after reaction; (c) C 1s and (d) O 1s XPS spectra of DBC900 after reaction.

$$\text{DBC900–C=O} + HSO_5^- + OH^- \rightarrow {}^1O_2 + SO_4^{2-} \quad (1)$$

$$\text{DBC900–Defects} + HSO_5^- + {}^{\bullet}OH \rightarrow O_2^{\bullet -} + SO_4^{2-} + 2H^+ \quad (2)$$

$$2O_2^{\bullet -} + 2H_2O \rightarrow {}^1O_2 + H_2O_2 + 2OH^- \quad (3)$$

$$\text{DBC900-PMS*} + \text{CIP} \rightarrow \text{intermediates} + SO_4^{\bullet -} \quad (4)$$

$$SO_4^{\bullet -} + H_2O \rightarrow {}^{\bullet}OH + SO_4^{2-} + H^+ \quad (5)$$

3.5. Degradation pathway of CIP

The degradation products of CIP in the DBC900/PMS system were analyzed by LC-MS, and the detected intermediates were summarized in Table S2. As illustrated in Fig. 9, the piperazine ring in CIP molecule ($m/z = 332$) was cleaved to form intermediate product of P1 ($m/z = 306$), Meanwhile, CIP was attacked by ROS to produce the intermediate P2 ($m/z = 330$) as a result of defluorination. Then, the defluorination of intermediate P1 and the piperazine ring cleavage of P2 resulted in the generation of P3 ($m/z = 304$). The hydroxyl group in P3 was shed to form P4 ($m/z = 288$). The intermediate P5 ($m/z = 245$) was generated by the further oxidation of piperazine ring in P4. The decarboxylation of P5 resulted in the formation of P6 ($m/z = 218$). P7 ($m/z = 178$) was generated through the elimination of cyclopropane. The hydroxyl group and amino group in P7 was shed to form P8 ($m/z = 146$). Finally, intermediate P8 was further degraded into small molecules *via* ring-opening and subsequently mineralized into CO_2, H_2O and NO_3^-.

Moreover, Toxicity Estimation Software Tool (T.E.S.T.) was employed to evaluate the toxicity of CIP and its intermediate products. As illustrated in Fig. S2, CIP, with the developmental toxicity of 1.09, was found to be "toxic". After the degradation by the DBC900/PMS system, the developmental toxicity of all the degradation products was reduced. Especially, the intermediates P3, P5 and P7 exhibited development non-toxicant.

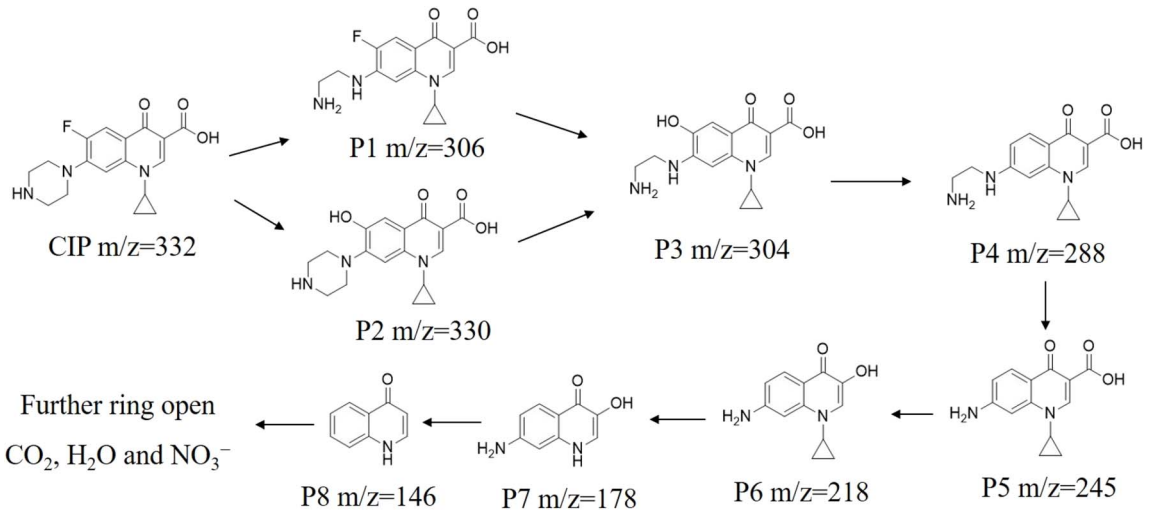

Fig. 9 Proposal degradation pathway of CIP in the DBC900/PMS system.

4. Conclusion

Herein, waste distillers' grains were utilized to prepare a high-performance biochar catalyst *via* high-temperature pyrolysis for enhanced CIP degradation in SR-AOPs. The DBC900 catalyst pyrolyzed at 900 °C demonstrated superb potential for activating PMS to degrade CIP in water. 100% CIP removal was achieved by the DBC900/PMS system within 40 min. This system also strongly resisted interference from inorganic ions and HA, and good performance was maintained across a wide range of pH levels. Notably, after five cycles of use, a CIP degradation efficiency of 86.6% was maintained by DBC900, emphasizing its suitability as a reusable catalyst. Scavenging and EPR analyses demonstrated that the reaction mechanism involved non-radical pathway and electron transfer pathway. The generation of $^1O_2$ and electron transfer mediated by the metastable complex DBC900-PMS* were crucially involved in degrading CIP. The transformation of waste distillers' grains into metal-free carbon nanomaterials provided a compelling method for utilizing and valorizing distillers' grains.

Conflicts of interest

There are no conflicts to declare.

Data availability

The corresponding author will provide access to all the data used to support this research upon receiving an adequate request.

Supplementary information (SI): Text S1: the detailed information including instruments and methods used in catalyst characterization; Fig. S1: the N_2 adsorption–desorption isotherms and the pore size distributions; Table S1: the parameters of different water bodies; Table S2: structures, retention times and molecular weight/charge (m/z) of the intermediates. See DOI: https://doi.org/10.1039/d6ra02077a.

Acknowledgements

The authors are grateful for the financial support from National Natural Science Foundation of China (22266030), Sichuan Science and Technology Program (2025YFHZ0312) and Department of Education of Guizhou Province (QJJ [2023]026).

References

1 H. Wang, X. Wu, J. Xu, Z. Lu, B. Hu, L. Zhu and H. Lu, *J. Hazard. Mater.*, 2025, **489**, 137561.
2 Y. Feng, D. Wu, Y. Deng, T. Zhang and K. Shih, *Environ. Sci. Technol.*, 2016, **50**(6), 3119–3127.
3 Y. Ding, X. Wang, L. Fu, X. Peng, C. Pan, Q. Mao, C. Wang and J. Yan, *Sci. Total Environ.*, 2021, **765**, 142794.
4 A. Hassani, J. Scaria, F. Ghanbari and P. V. Nidheesh, *Environ. Res.*, 2023, **217**, 114789.
5 H. V. Lutze, N. Kerlin and T. C. Schmidt, *Water Res.*, 2015, **72**, 349–360.
6 T. Zhang, P. Yang, Y. Ji and J. Lu, *Environ. Sci. Technol.*, 2025, **59**, 3325–3335.
7 B. Barrios, B. Mohrhardt, P. V. Doskey and D. Minakata, *Environ. Sci. Technol.*, 2021, **55**, 8054–8067.
8 Y. Bu, H. Li, W. Yu, Y. Pan, L. Li, Y. Wang, L. Pu, J. Ding and G. Gao, *Environ. Sci. Technol.*, 2021, **55**, 2110–2120.
9 C. Zhang, H. Wu, F. Cheng and J. Li, *J. Environ. Chem. Eng.*, 2025, **13**, 119502.
10 Y. Gao, Z. Chen, Y. Zhu, Li Tong and C. Hu, *Environ. Sci. Technol.*, 2020, **54**, 1232–1241.
11 Q. Kuai, Y. Wang, J. Yang, T. Huang, Y. Guan, Z. Liu and J. Ma, *Purif. Technol.*, 2025, **364**, 132396.
12 S. A. Abdalla, F. S. Mustafa, K. H. H. Aziz, S. J. Mohammed and D. A. Kader, *RSC Adv.*, 2025, **15**, 42843–42856.
13 H. Dong, H. Liang, L. Yang, X. Yang, C. Yang, G. Hu and T. Zhao, *J. Environ. Chem. Eng.*, 2023, **11**, 110137.
14 X. Xu, W. Feng, L. Guo, X. Huang and B. Shi, *Sci. Total Environ.*, 2023, **867**, 161382.

15 Y. Da, M. Xu, J. Ma, P. Gao, X. Zhang, G. Yang, J. Wu, C. Song, L. Long and C. Chen, *Ecotoxicol. Environ. Saf.*, 2023, **262**, 115171.
16 B. Wang, G. Lian, X. Lee, B. Gao, L. Li, T. Liu, X. Zhang and Y. Zheng, *Chemosphere*, 2020, **238**, 124684.
17 Q. Xu, T. Liu, L. Li, B. Liu, X. Wang, S. Zhang, L. Li, B. Wang, A. R. Zimmerman and B. Gao, *Bioresour. Technol.*, 2021, **340**, 125725.
18 X. Liu, Z. Shao, Y. Wang, Y. Liu, S. Wang, F. Gao and Y. Dai, *Environ. Res.*, 2023, **216**, 114651.
19 H. Dong, H. Liang, L. Yang, X. Yang, C. Yang, G. Hu and T. Zhao, *J. Environ. Chem. Eng.*, 2023, **11**, 110137.
20 D. Ouyang, Y. Chen, J. C. Yan, L. B. Qian, L. Han and M. F. Chen, *Chem. Eng. J.*, 2019, **370**, 614–624.
21 D. Ouyang, Y. Chen, R. H. Chen, W. Y. Zhang, J. C. Yan, M. Y. Gu, J. Li, H. B. Zhang and M. F. Chen, *Sci. Total Environ.*, 2022, **809**, 151929.
22 Y. M. Huang, G. Li, M. Z. Li, J. J. Yin, N. Meng, D. Zhang, X. Q. Cao, F. P. Zhu, M. Chen, L. Li and X. J. Lyu, *Sci. Total Environ.*, 2021, **754**, 141999.
23 M. Cai, L. Dai, Y. Huang, Y. Xie, Y. Zhang and Y. Wang, *Ind. Crops Prod.*, 2024, **221**, 119402.
24 T. Wang, H. Liu, C. Duan, R. Xu, Z. Zhang, D. She and J. Zheng, *Mater.*, 2020, **13**, 3391.
25 B. Chen, D. Zhou and L. Zhu, *Environ. Sci. Technol.*, 2008, **42**, 5137–5143.
26 Y. Chen, G. Zhang, H. Liu and J. Qu, *Chem. Int. Ed. Engl.*, 2019, **58**, 8134–8138.
27 D.-G. Kim and S.-O. Ko, *Chem. Eng. J.*, 2020, **399**, 125377.
28 J. Yan, Q. Meng, X. Shen, B. Chen, Y. Sun, J. Xiang, H. Liu and B. Han, *Sci. Adv.*, 2020, 1951.
29 Li-M. Chiang, T.-B. Nguyen, C.-W. Chen, C.-Di Dong b and C.-H. Wu, *J Water Process Eng*, 2025, **76**, 108218.
30 P. Sun, K. Zhang, J. Gong, A. Khan, Y. Zhang, M. S. Islama and Y. Zhang, *Environ. Sci. Pollut. Res.*, 2019, **26**, 27482–27493.
31 J. Wang and S. Wang, *Chem. Eng. J.*, 2018, **334**, 1502–1517.
32 X. Miao, X. Chen, W. Wu, D. Lin and K. Yang, *Chem. Eng. J.*, 2022, **438**, 135606.
33 M. Zhang, C. Han, W. Chen, W. Luo, Y. Cao, G. Qian, X. Zhou, X. Duan, S. Wang and X. Duan, *Green Energy Environ.*, 2020, **5**, 444–452.
34 X. Pei, X. Peng, X. Jia and P. K. Wong, *J. Hazard. Mater.*, 2021, **419**, 126446.
35 B. Byambaa, E.-J. Kim, M. G. Seid, B.-M. An, J. Cho, S. L. Aung and K. G. Song, *Chem. Eng. J.*, 2023, **456**, 141037.
36 X. Cheng, H. Guo, Y. Zhang, X. Wu and Y. Liu, *Water Res.*, 2017, **113**, 80–88.
37 H. Sun, C. Kwan, A. Suvorova, H. M. Ang, M. O. Tadé and S. Wang, *Appl. Catal. B*, 2014, **154–155**, 134–141.